analytical chemistry

pubs.acs.org/ac Article

Exploiting Photoelectric Activities and Piezoelectric Properties of $NaNbO_3$ Semiconductors for Point-of-Care Immunoassay

Zhichao Yu, Hexiang Gong, Jianhui Xu, Yuxuan Li, Yongyi Zeng, Xiaolong Liu,* and Dianping Tang*

Cite This: *Anal. Chem.* 2022, 94, 3418−3426 Read Online

ACCESS | Metrics & More | Article Recommendations | Supporting Information

ABSTRACT: Point-of-care testing (POCT) technology has made major breakthroughs in community medicine and physician office situations, in tandem with the more ubiquitous and intensive usage of highly integrated quick detection equipment for illness diagnosis, personal care, and mobile healthcare. Although the photoelectrochemical (PEC)-based POCT platform offers the benefits of cheap cost and good user engagement, its commercialization is still limited by the photodetection components' downsizing and mobility, among other factors. In this work, a novel highly integrated PEC biosensor aided by piezophototronics to enhance the efficiency of PEC testing was reported for flexible detection of cancer-associated antigens in biological fluids (prostate-specific antigen, PSA, used as an example). Multiple signal enhancement strategies, including a magnetic bead-linked enzyme-linked immune system catalyzing the production of ascorbic acid from the substrate and a piezoelectric-assisted enhancement strategy, were used for sensitive detection of the analyte to be tested in human body fluids. Unlike the electron transfer mechanism in heterojunctions, piezoelectric semiconductors promote the transfer of electrons and holes by generating piezoelectric potentials in the ultrasonic field, thus contributing to the performance of the PEC testbed. Under optimized conditions, the test platform achieves good correspondence for PSA at 0.02−40 ng mL^{-1}. Impressively, the test devices are comparable to or even superior to gold standard ELISA kits in terms of cost approval and batch testing. This research demonstrates the potential of piezoelectric semiconductors for POC applications in revolutionary PECs and offers innovative thoughts for the development of new PEC bioanalytical components.

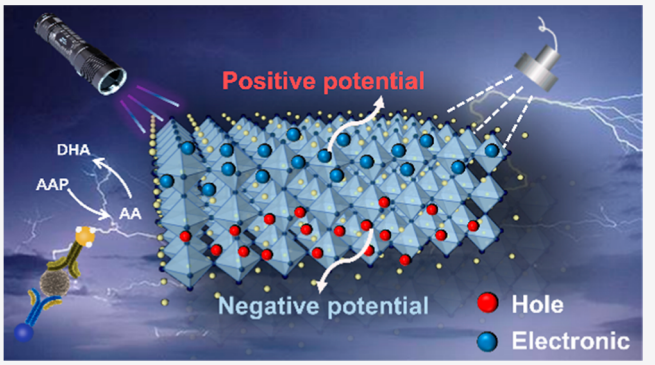

Photoelectrochemical (PEC) bioanalysis technology, as a branch of electrochemical analysis, has recently drawn a lot of attention from researchers due to its good stability and excellent analyte response.[1−7] As the central element in PEC testing, suitable photoelectrodes are used to build the bridge between light and electricity to identify special probes and prebuilt biological events. The ideal PEs are considered to exhibit effective photoresponse and signal conversion, suitable biocompatibility, and the ability to generate stable photocurrents.[8] Photosensitive materials, including inorganic semiconductors and organic materials, such as the classical inorganic semiconductors TiO_2[9−11] and CdS,[12−14] as well as metal−organic framework ZIF-based derivatives,[15,16] have been developed to meet the testing needs of PEC in a variety of situations. For example, Zhang et al. reported a series of carbon materials including C_{60}, graphite, nitrogen carbide, graphene, and other advanced functional materials, through the appropriate biological interface engineering to build a strong PEC biosensing platform.[17−21] Previously, we have also proposed a layer-by-layer assembly of ferroelectric-mediated electron−hole transfer schemes consisting of photoelectrical semiconductors and ferroelectric perovskite.[22] Similarly, Yu et al. reported the feasibility of an auxiliary strategy for ferroelectric induction to enhance the efficiency of photogenerated electrons and holes.[23]

Piezoelectric materials are capable of generating spontaneous built-in potential differences through external pressure fields and have attracted extensive attention in the fields of PEC and photocatalysis as photoelectrical materials and related energy harvesting systems.[24−28] Among the large family of piezoelectric chalcogenides, $NaNbO_3$ exhibits great PEC activity and controllable complexation rate of photogenerated charge carriers. Meanwhile, the green synthesis of $NaNbO_3$ enables it to be a candidate to replace conventional semiconductors such as TiO_2 and ZnO in the field of PEC. Liu et al. constructed nanodomain $NaNbO_3$ with a localized structure and polar heterogeneity for high-performance piezoelectric materials for electromechanical sensor and

Received: January 6, 2022
Accepted: February 2, 2022
Published: February 11, 2022

https://doi.org/10.1021/acs.analchem.2c00066
Anal. Chem. 2022, 94, 3418−3426

Scheme 1. Fully Integrated CAAB; (A) Schematic Diagram of the PEC Platform; The Platform Includes an Integrated Four-Microelectrode System, a Flow Feeder, a Magnetic Separation Incubation Platform, an Analogue-To-Digital Conversion Platform, and a Signal Output Device; (B) Principle of Testing for Low Abundance Cancer Markers is Explored in This Report with Prostate-Specific Antigen (PSA) (a Prostate Cancer-Related Marker) as a Feasibility Study; (mAb_1: Monoclonal Anti-PSA Capture Antibody; mAb_2: Monoclonal Anti-PSA Detection Antibody; SiO_2: Silicon Dioxide; and ALP: Alkaline Phosphatase)

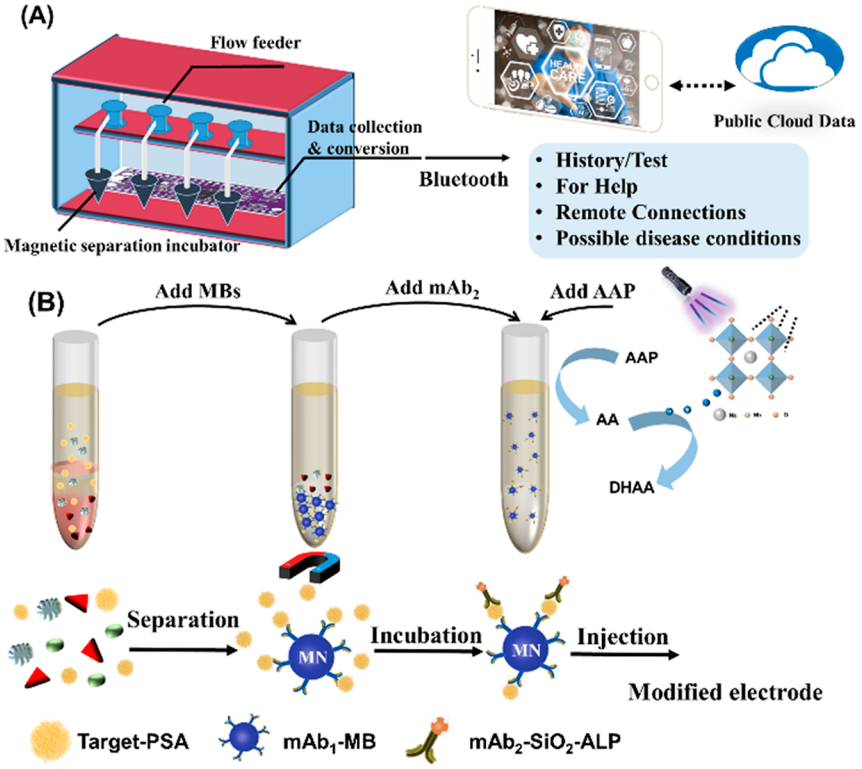

actuator applications.[29] Logically analyzed, similar piezoelectric materials with piezoelectric activity and photoelectrical semiconductor properties such as $NaNbO_3$ can be used to be photoanodes. Regrettably, there are likely no reports or explorations on piezoelectric materials in the field of PEC bioanalysis. In other words, it is entirely possible to build powerful piezoelectric effect photoelectrical semiconductors to complete a delicate PEC sensing platform.

A complete and refined biosensing protocol should have good analyte response and stability, but more importantly, portable design and low cost and scale of production are of higher concern to the researchers and testers.[30,31] Based on the principle that less is more, researchers have replaced traditional PEC test systems with components such as auto-sampling devices,[32−34] microfluidic platforms,[35−38] and 3D printing equipment[39−43] to meet the demand for miniaturized and portable assays. More meaningfully, with the booming development of microcontroller technology, more studies have proposed microcontroller-based signal transduction and processing as an alternative to electrochemical workstations, providing a portable and good user-interactive platform for achieving sensitive and multichannel real-time analysis. For example, we reported on the use of a flexible microcontroller to detect visualized currents in a previous study of a portable pressure-sensitive biosensor platform.[44]

Herein, we report a portable cancer-related antigen assay box (CAAB) with a fully integrated piezoelectric generation device and miniature PEC test platform. Briefly, the CAAB platform integrated a micro-auto sampling device, a magnetic bead target separation system, a 3D printing-based detection cell, a set of paper-based capacitors, and UV light beads to replace the traditional PEC platform for completing the detection of target antigens. The CAAB platform was not limited by bulky PEC test instruments, and costs were kept within acceptable limits for most point-of-care testing (POCT). Scheme 1 briefly describes the principle of CAAB testing and the related model building. Binding of target and capture antibodies occurred in microtubules, followed by the formation of magnetic bead-type immune complexes with enzyme-labeled SiO_2 nanoparticles that were separated by an external magnetic field and catalyzed the oxidation of the substrate to produce ascorbic acid (AA). The piezoelectric photoelectric material $NaNbO_3$ experienced directional carrier movement under UV light irradiation, and the external force field intensified the separation efficiency of electrons and holes, and also enhanced the mixing of the low and high concentrated sacrificial agent regions of the electrode, resulting in a relatively stable and apparent current change. In addition, the collection of photocurrent was done by a homemade paper supercapacitor, which was charged and instructed to release current, and the obtained instantaneous current was recorded by a built-in electrical element and sent to the output of the smartphone terminal. More importantly, the multiwell design was expected to allow multiple analyses of multiple carcinoembryonic antigens or a single detector to expand the application scenario. This work not only describes the potential capabilities of piezoelectric materials in PEC detection but also provides a fully integrated PEC bioassay platform with a detection process that does not require additional instrumentation and trained personnel, not to

https://doi.org/10.1021/acs.analchem.2c00066
Anal. Chem. 2022, 94, 3418−3426

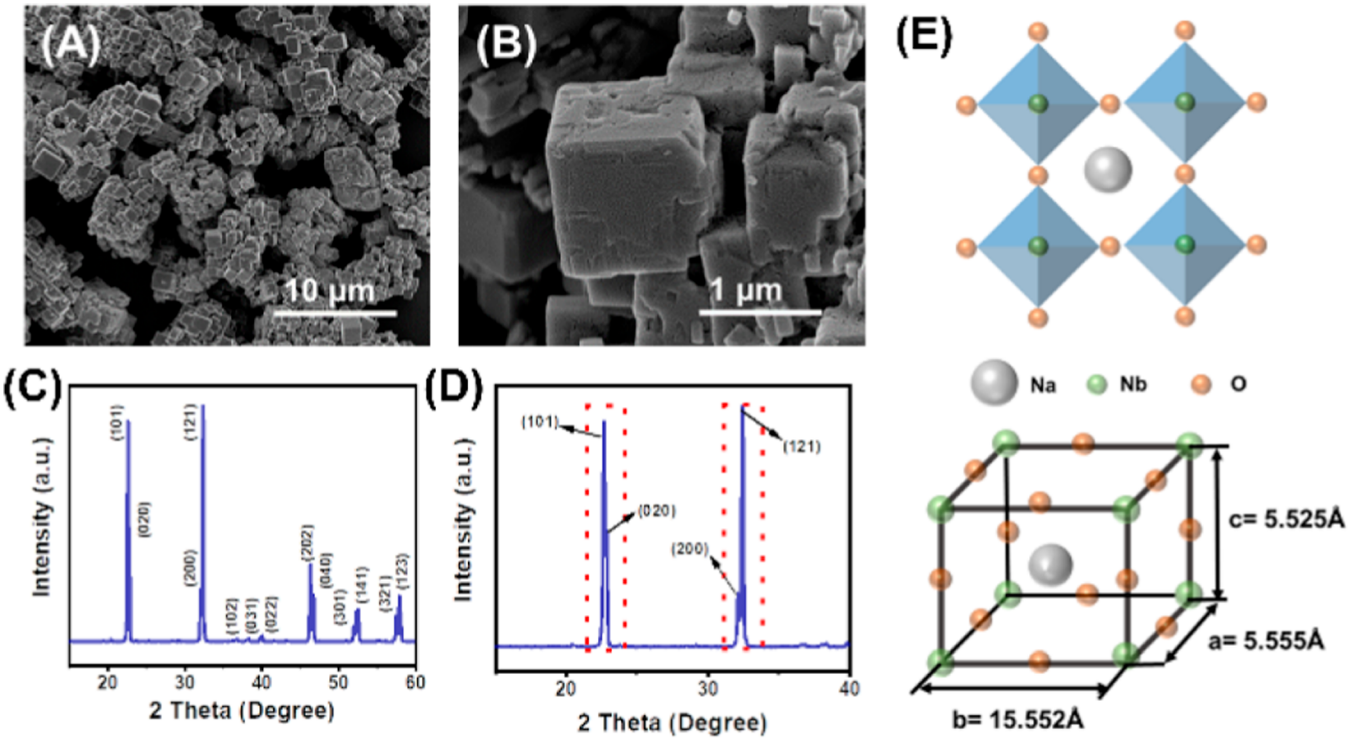

Figure 1. (A,B) SEM images of $NaNbO_3$ at low magnification and high magnification. (C) XRD patterns and (D) refinement patterns of $NaNbO_3$. (E) Structural analysis of nanocubic $NaNbO_3$.

mention signal differences due to electrode differentiation, promising the commercialization of low-abundance tumor marker detection.

EXPERIMENTAL SECTION

Synthesis of Piezoelectric $NaNbO_3$ Nanosemiconductor. Nanostructured semiconductor $NaNbO_3$ was synthesized based on alkaline hydrolysis by the one-pot method.[45] Briefly, 0.0023 mol of niobium oxide (Nb_2O_5) was dissolved in 80 mL of deionized water. After complete dissolution, 0.24 mol of sodium hydroxide was added to adjust the pH to promote hydrolysis under alkaline conditions and stirred at moderate speed for 2 h for the complete dissolution of the solute. Afterward, the white incomplete clear solution was transferred to a 120 mL polytetrafluoroethylene (PTFE)-lined hydrothermal kettle and underwent heat treatment (150 °C, 48 h) in an oven. The product was washed several times with deionized water and ethanol and collected by centrifugation.

Construction of CAAB and Testing Protocols. Schematic diagrams of the 3D construction of the test box and the electronic modules built for data collection and processing are shown in Scheme 1A. The outer shell layer of CAAB was made of polymethyl methacrylate which was laser cut to the designed shape and assembled through the slot to complete the assembly. The testing process and principle of the microcontroller-based multiple capacitor discharge current monitoring system are shown in Figure S1. Focusing on the capacitor bank charging and discharging circuit, the capacitor bank discharging current data acquisition device is mainly concerned with charging and discharging control and the dynamic monitoring of the electrical signals during this process. In the actual assembly and considering the operability, the monolithic structure 806 microcontroller was chosen as the main device to collect and control the charging and discharging of the capacitor bank. The minimum system circuit is made by a double panel, mainly divided into three parts, that is crystal circuit, reset circuit, and power supply circuit of the microcontroller, as shown in Figure S2.

The PEC core test system with working electrodes is shown in Figure S3, and the device could be completed with the assistance of 3D printing. Briefly, Cu sheets were used to load piezoelectric nanomaterials. A 10 μL solution of $NaNbO_3$ isopropanol (10 mg mL^{-1}) was added dropwise to the microelectrode area and dried in an oven at 60 °C. Notably, a few drops of Nafion solution was added to this solution to improve the adhesion of the nanostructures to the substrate; otherwise, the electrodes would fall off and cause the current to drift or even short circuit. The abovementioned steps were repeated three times. The working electrode should be completely sonicated before the test to prevent errors due to the detachment of the electrode material during the piezoelectric photoelectric synchronous test. All tests were performed at room temperature. The ultrasonic test procedure was performed in a CNC ultrasonic cleaner (KQ5200DE, Kunshan, China). If not otherwise specified, the tests were performed at 90% of maximum power.

Immunoassay Procedures and PEC Detection. Scheme 1B provides a brief description of the rationale for the PEC test platform for cancer markers (with PSA as the target to be measured), and details of the preparation of capture and recognition antibodies and other experimental information are expressed in the Supporting Information. A host of PTFE hoses were used to connect the reagent bottles to the incubation cell, and with the aid of a syringe pump, the flow assay cell was filled with the incubation solution. The flow direction and flow rate were controlled by the valve and the syringe pump, respectively. The PSA bio-recognition and signal transduction process were briefly described as follows:

https://doi.org/10.1021/acs.analchem.2c00066
Anal. Chem. 2022, 94, 3418−3426

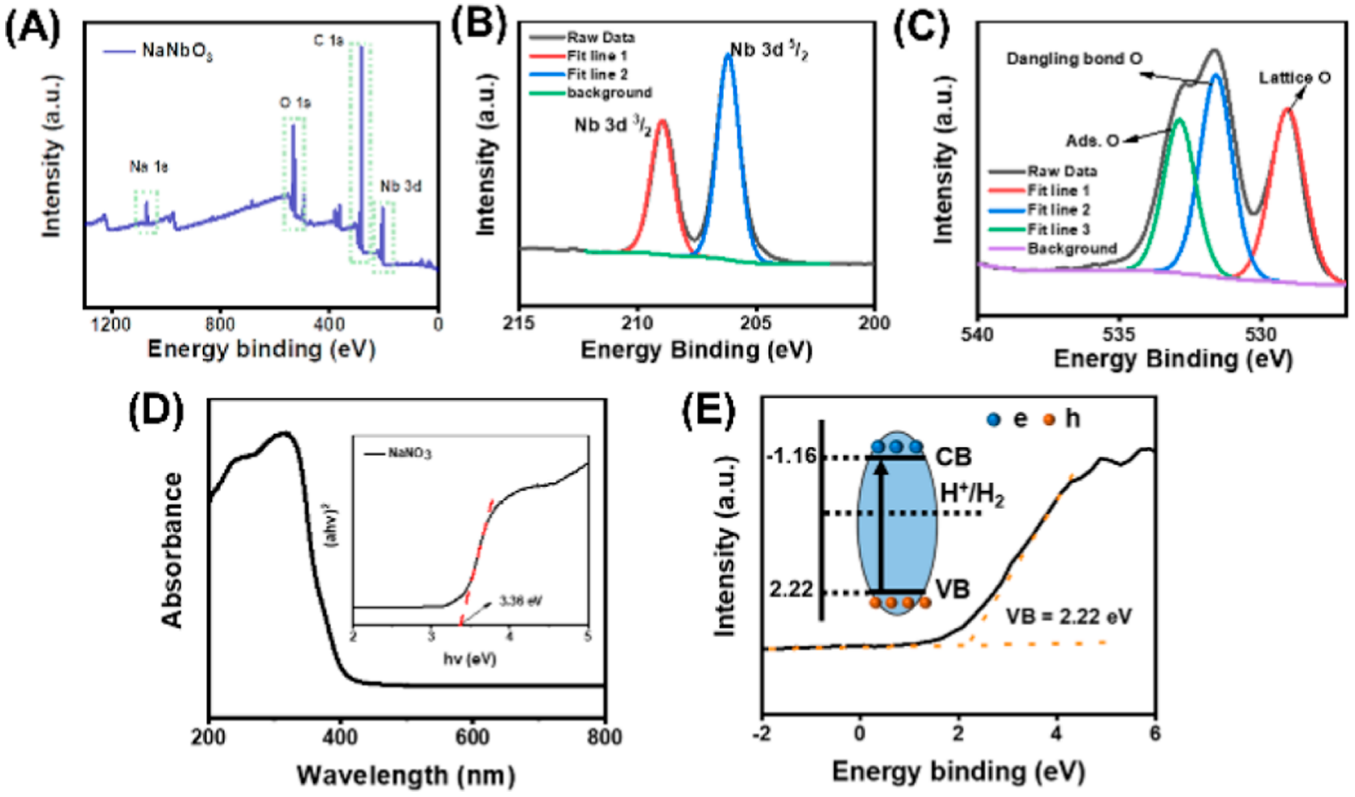

Figure 2. (A,B) XPS survey spectra, (B) Nb 3d, and (C) O 1s high-resolution spectra of $NaNbO_3$. (D) UV diffuse reflectance spectrum of nanocubic $NaNbO_3$. Inset: the band gap spectrum of the material calculated using Kubelka–Munk function. (E) VB spectral test results of $NaNbO_3$.

(i) 100 μL of mAb_1-MN immunoprobe was injected by selecting the corresponding six-way valve (800 μL min^{-1}) and then switching the valve to inject 100 μL of mAb_2–SiO_2–ALP for the formation of sandwich immune complexes. The incubation cell contained 100 μL of a specific concentration of PSA or a different sample to be tested. (ii) 500 μL of phosphate-buffered saline (PBS) buffer was used to wash the incubation cell to remove unreacted biomolecules; this process needs to be performed with the assistance of a magnet. (iii) Afterward, 1.0 mM AAP was added to the incubation cell and incubated at 35 °C for 1 h. The enzymatic digestion product (AA) of ALP was transferred to the homemade assay cell. The photoelectric signal was collected by a paper-based supercapacitor under the excitation of UV light beads. Paper-based supercapacitors are made in the same way as we reported earlier.[46] The photocurrent at the workstation was recorded by a three-electrode system, if not otherwise specified. Controlled by a microcontroller, the recorded current was released instantaneously and the sensor signal was recorded on the smartphone. After completion of the assay, the PBS wash solution was passed into the incubation and detection cell. All actual serum samples need to be subjected to a 10 min (6000*g*) centrifugation procedure prior to incubation to remove the possible precipitate.

RESULTS AND DISCUSSION

Morphology and Structure of Piezoelectric $NaNbO_3$ Nanomaterials. One of the most critical aspects of the construction of the PEC analysis equipment is the successful synthesis and characterization of the photoelectrodes. In this work, the photoelectric piezoelectric semiconductor $NaNbO_3$, which has good photoelectric conversion efficiency, is chosen as the photoelectric electrode because of its good chemical stability, excellent piezoelectric photoelectric properties, and so forth. At first, the morphology of the hydrothermally synthesized $NaNbO_3$ was measured by scanning electron microscopy (SEM). The SEM results showed that the synthesized $NaNbO_3$ has a homogeneous nanocubic morphology (Figure 1A). $NaNbO_3$ at high magnification indicated an angular cubic structure with a size of about 1 μm, as shown in Figure 1B. To verify the successful synthesis of piezoelectric $NaNbO_3$, the X-ray diffraction (XRD) test pattern results shown in Figure 1C,D is used. The XRD results showed the successful synthesis of the single phase of $NaNbO_3$ nanostructure and the double peaks indicated that the synthesized single phase was of orthogonal crystal type. Meanwhile, the XRD-refined Rietveld data indicated that the *abc*-axis lengths of individual lattices were 5.555, 15.552, and 5.525 Å, respectively, while indicating that the synthesized nanocube-like $NaNbO_3$ was a ferroelectric phase semiconductor with a P_2ma dot group. Figure 1E shows the single-crystal structure and corresponding parameters of the synthesized nanocubes. The relevant information refined and calculated by refinement of the XRD patterns is represented in Figure S4. The crystal structure characterization of $NaNbO_3$ nanocubes was obtained by further Raman spectroscopy studies. As shown in Figure S5, pure $NaNbO_3$ suggested multiple signal vibration peaks at 130 and 220 cm^{-1}, which was mainly due to the translational vibration modes of Na. The vibration peaks appearing at 450 and 625 cm^{-1} in the test result curves were assigned to the stretching vibration of Nb–O. In addition, several vibrational bands such as those at 126

https://doi.org/10.1021/acs.analchem.2c00066
Anal. Chem. 2022, 94, 3418–3426

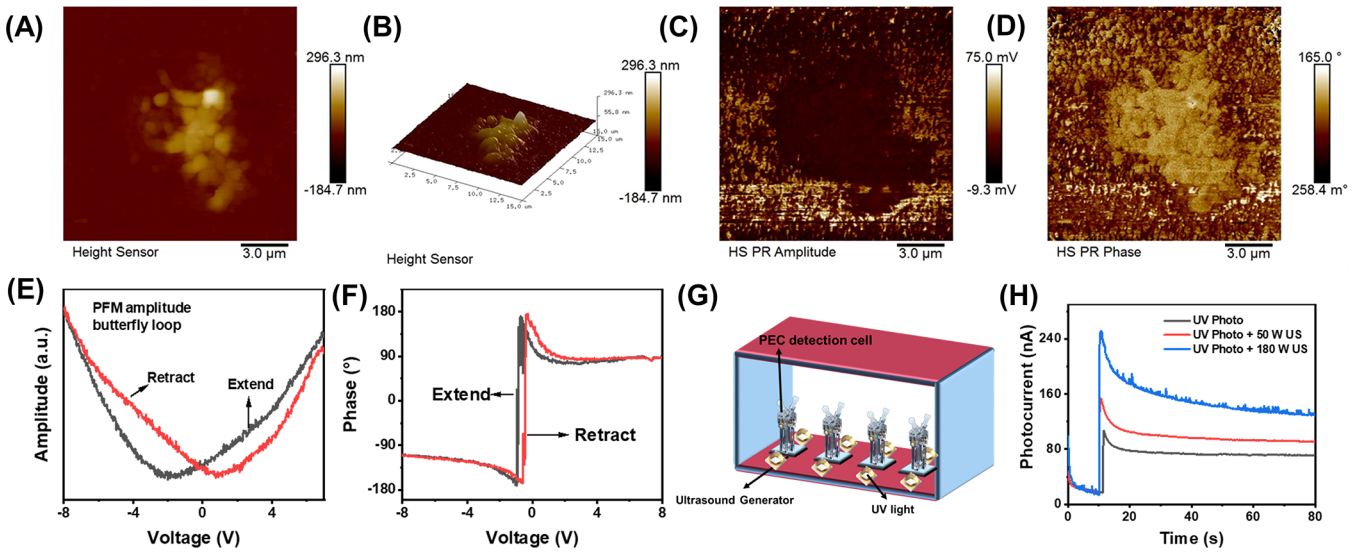

Figure 3. (A) AFM images of $NaNbO_3$ nanomaterials. (B) Three-dimensional height image of the corresponding area. (C) Amplitude variation graph and (D) phase change diagram for the corresponding region. PFM amplitude butterfly loop and (F) phase hysteresis loop of $NaNbO_3$ nanostructure. (G) Schematic diagram of a PEC test bench with UV beads and ultrasound generators. (H) Photocurrent response images under a UV lamp and ultrasound conditions.

and 142 cm^{-1} were associated with the vibration of the octahedron of NbO_6, which would produce most of the peaks around 160 cm^{-1}. Expectedly, the octahedral NbO_6 would show a Raman signal at 600 cm^{-1} due to the typical stretching vibration mode.

Characterization of Photoelectric Response of $NaNbO_3$ Nanomaterials. To further investigate the photoelectric responsiveness of $NaNbO_3$, X-ray photoelectron spectroscopy (XPS) and UV diffuse reflectance were used to determine its photoelectric response. The surface composition and valency of the synthesized $NaNbO_3$ nanorods were determined by XPS, where the binding energy of surface carbon elements (C 1s = 284.8 eV) was used as a reference. The result of the measurements is shown in Figure 2A, indicating the presence of Na, Nb, and O elements in the synthesized nanomaterials and the absence of other impurity contamination peaks paired to the electron binding energy of the known elements. The result of the high-resolution spectra corresponding to Nb 3d is shown in Figure 2B, where the wave peaks of 209.0 and 206.2 eV were assigned to Nb $3d_{3/2}$ and Nb $3d_{5/2}$, respectively, which confirmed the presence of Nb elements in $NaNbO_3$ in the form of Nb^{5+}. As shown in Figure 2C, by deconvolution of the high-resolution spectra of O 1s, it was found that the presence of O in the lattice could be assigned to the lattice oxygen, surface adsorbed oxygen, and free oxygen, where surface adsorbed oxygen and free oxygen could be considered as the presence of oxygen vacancies in the lattice structure of $NaNbO_3$, which had been confirmed in previous reports.[47]

To further confirm the successful synthesis of $NaNbO_3$ and the extent of its response to light, the UV−vis diffuse reflectance spectrum of nanomaterials is indicated in Figure 2D. The test results showed that the fabricated nanomaterials exhibited good absorption of UV light from 200 to 400 nm. Further, the band gap of the tested $NaNbO_3$ is expressed in the inset of Figure 2D by the Tauc relation transformation, and the results demonstrated that extrapolating the linear part of the curve between $(\alpha h\nu)^2$ and $(h\nu)$ to zero, a band gap value of ∼3.36 eV was obtained, which was consistent with previous studies.[45] In addition, experimental data for determining the specific positions of the conduction band (CB) and valence band (VB) of $NaNbO_3$ were obtained in the XPS test (Figure 2E). The VB position of about 2.22 eV was obtained by reasonable extrapolation and calculation, and the CB position of −1.16 eV was obtained by combining the test results of Figure 2D, and the data visualization is shown in the inset of Figure 2E. Such a low CB position (0.36 eV lower compared to ZnO) was more suitable for the transfer of electrons in the PEC process.[48,49] Up to this point, we have demonstrated the possible photoelectric and piezoelectric potential of the semiconductor nanomaterial $NaNbO_3$.

Piezoelectric Responsiveness of $NaNbO_3$. Another point to be explored is whether the synthesized nanocubes $NaNbO_3$ are piezoelectric. To characterize the ferroelectric/piezoelectric properties in $NaNbO_3$ nanocrystals, piezoelectric response force microscopy (PFM) was used to probe the piezoelectric response of the coated indium-tin-oxide substrate film by applying a bias voltage (±8 V). Initially, we determined the specific location and morphology of $NaNbO_3$ by the tap pattern of atomic force microscopy (AFM). As shown in Figure 3A,B, the AFM test results indicated that the height difference of the selected region was about 400 nm, which was consistent with the results obtained by SEM in Figure 1A, indicating that the region was a stacking of nanocubes of $NaNbO_3$. The PFM amplitude and phase images are presented in Figure 3C,D, from which it was clear that the material region had undergone an amplitude and phase change in response to external stimuli, indicating that the nanoscale domains in this region were considered to be piezoelectric. In addition, as shown in Figure 3E, the polarization butterfly ring of the PFM revealed that the $NaNbO_3$ semiconductor film exhibited good piezoelectricity, which also indicated the semiconducting nature of $NaNbO_3$. The complete flip of the $NaNbO_3$ phase occurs with −0.3 V. The phase hysteresis also suggested the good piezoelectricity of the characterized films. To visually represent the piezoelectric response of the material, an alternating current (AC) voltage applied between the probe and the substrate caused periodic expansion and contraction or

https://doi.org/10.1021/acs.analchem.2c00066
Anal. Chem. 2022, 94, 3418−3426

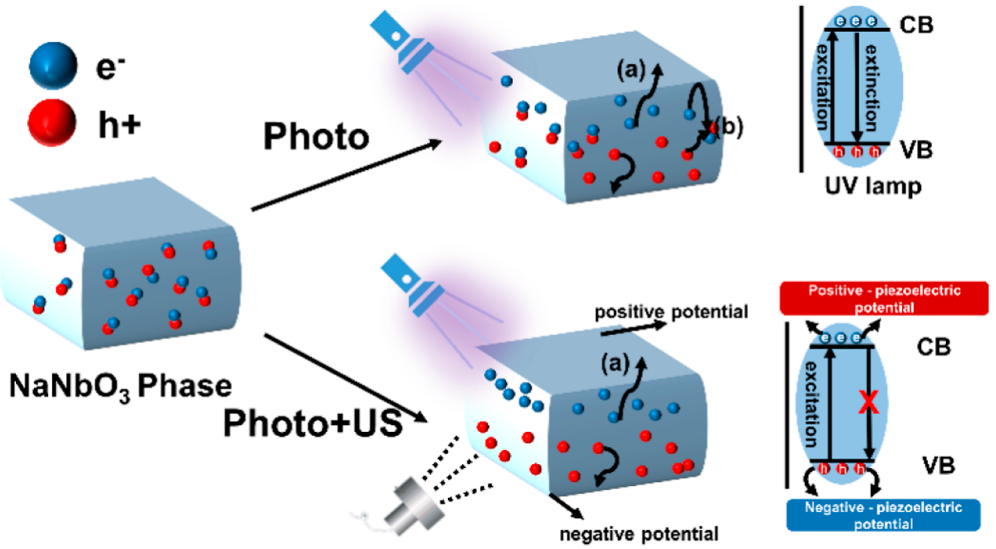

Figure 4. Schematic diagram of the piezoelectric enhancement effect mechanism of $NaNbO_3$ nanocubes.

phase flip of the sample, as shown in Figure 3F. $NaNbO_3$ exhibited two regions of low and high phases after applied voltage with distinct boundaries, which demonstrated that the material was piezoelectric.

To investigate the potential of the piezophototronic effect of $NaNbO_3$ for PEC testing, ultrasonic vibration models under dark and UV excitation were constructed to evaluate this effect for PEC testing, as shown in Figure 3G. We performed incubation tests with 5.0 ng mL^{-1} of PSA in an incubation cell and transferred the enzyme-linked immunocatalyzed product AA to the test system, as further expressed in the specific experimental section in the Supporting Information. As shown in Figure 3H, the generated photocurrent was stable under either the presence or absence of ultrasound, and there was no cliff-down drop, which indicated that the electrode material $NaNbO_3$ was stable at the electrode. The catalytically generated AA as a light sacrificial agent exhibited a photocurrent of about 80 nA when excited only by UV light. The photocurrent appears to be significantly enhanced when the ultrasound field was introduced (red line), and it changed as the intensity of ultrasound increased (blue line). This enhancement of photoelectric activity was directly related to the piezophototronic effect. To verify whether the ultra-temporal ultrasound causes the displacement of $NaNbO_3$ attached to the electrode surface, the stability of the electrode under cyclic ultrasound switching was verified, as shown in Figure S6. After 400 s ultrasound/UV switching experiments under 50 W ultrasound conditions, it could be seen that the change in photocurrent was negligible and the negligible current drawdown might be due to the photo-redox process of AA generated by enzyme-linked catalysis.

The working mechanism of the piezoelectric material $NaNbO_3$ used to improve the effectiveness of the PEC working platform under periodic ultrasonic vibration is schematically shown in Figure 4. In brief, the enhanced PEC test platform was based primarily on the piezophototronic effect. In the synthesized nanocubic $NaNbO_3$, the interior undergoes periodic exogenous ultrasonic vibrations to generate mechanical strain, which in turn induces spontaneous piezoelectric potentials. Under the excitation conditions of UV light, the separation of electrons and holes occurs, manifesting as the *a* pathway in the bulk phase, which carries electrons and holes away from the surface of the bulk phase for an effective redox reaction. In fact, electrons and holes prefer to be recombined in the bulk phase, as shown in the *b* pathway. The piezoelectric potential induced by ultrasound leads to an effective separation of photogenerated electrons/holes and inhibits the process of recombination in the bulk phase. Furthermore, because ultrasound is more advantageous for the diffusion of AA and the transfer to the low concentration region of the electron region, this also accelerates the further dissipation of electrons and holes. In conclusion, the introduction of ultrasonic fields in the PEC test process will provide a dramatic improvement both in terms of the piezophototronic effect and the accelerated diffusion of ultrasound. The reaction mechanism of piezoelectric photocatalytic substrates can be described as follows:

$$NaNbO_3 + h\nu + \text{ultrasonic vibration} \rightarrow h^+_{(VB)} + e^-_{(CB)} \quad (1)$$

$$e^-_{(CB)} + O_2 \rightarrow O_2^{-\bullet} \quad (2)$$

$$O_2^{-\bullet} + H_2O \rightarrow HO_2^{\bullet} + OH^- \quad (3)$$

$$h^+_{(CB)} + OH^- \rightarrow OH^{\bullet} \quad (4)$$

$$HO^{\bullet} + AA + HO_2^{\bullet} \rightarrow DHAA + H_2O + O_2 \quad (5)$$

Dose Response of the Piezo-Assisted Enhanced Platform for Target PSA. Standard dose testing of target PSA was performed on a constructed portable PEC test platform, and the experimental operations and associated optimization procedures for the incubation portion are indicated in the Supporting Information. Briefly, units of capture antigen, signal antigen, and target to be measured were continuously injected into the detection cell under the control of an autosampling device and then separated by a magnetic separation technique. Subsequently, by controlling a six-way valve, the substrate AAP was injected into the incubation cell for incubation and the obtained incubation product was transferred to the photoelectric detection cell. The assay was performed under ultrasonic and UV light conditions, as shown in Figure 5A. The change curves of photocurrent caused by

https://doi.org/10.1021/acs.analchem.2c00066
Anal. Chem. 2022, 94, 3418−3426

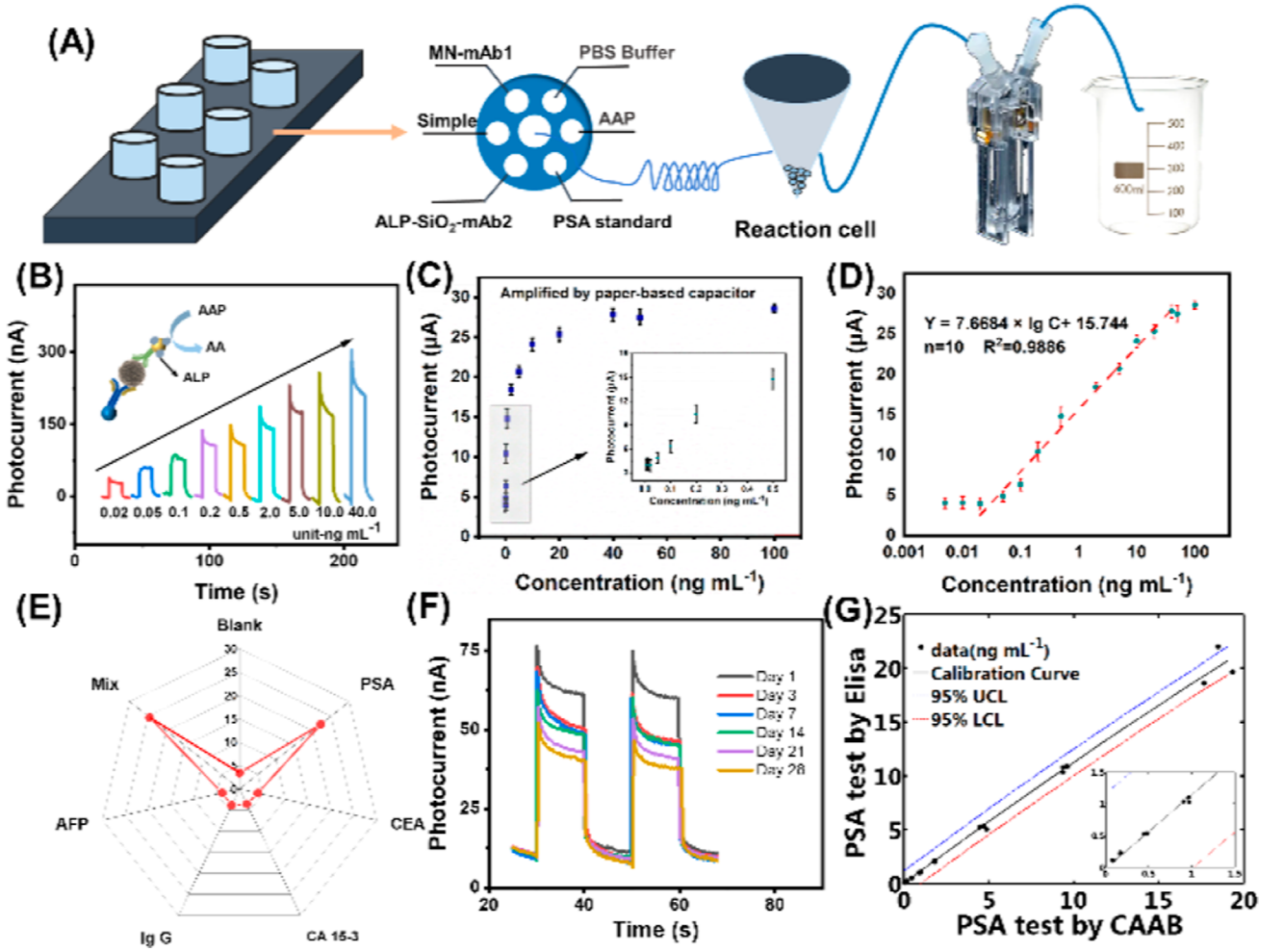

Figure 5. (A) Schematic diagram of the test procedure for a piezoelectric enhanced PEC sensor coupled to an autosampling device. (B) Photocurrent of the PEC platform for different concentrations of PSA standards (0.02 to 40.0 ng mL^{-1}). (C) Calibration plot of photocurrent response amplified by capacitor vs target PSA. (E) Selectivity of the PEC biosensor for PSA (4.0 ng mL^{-1}) vs carcinoembryonic antigen (CEA) (40 ng mL^{-1}), CA 15−3 (40 U mL^{-1}), immunoglobulin G (IgG) (40 ng mL^{-1}), and alpha-fetoprotein (AFP) (40 ng mL^{-1}). (The mixture consists of all the abovementioned interferences together). (F) Stability evaluation of photoelectric devices. (G) Correlation of CAAB with the Elisa kit for spiked recovery test, where the blue and red lines indicated the data distribution thresholds within plus or minus 5% deviation, respectively.

different doses of PSA are shown in the Figure 5B. It was obvious that the photocurrent tended to increase with the growth of target PSA, which was mainly controlled by the dissipation of AA in the photocatalytic process. The results of the test without charge collection through the capacitor are shown in Figure S8. Multiple measurements and processing of the raw data revealed that the target PSA concentration showed a positive correlation with a stable value of photocurrent, and a good linear relationship between photocurrent and PSA concentration could be fitted in the dynamic range from 0.02 to 40 ng mL^{-1}, as shown in Figure 5B,C. The integrated multifunctional test chip enables simultaneous control of paper-based capacitor charging and discharging, with charging time set to 70 s, in conjunction with optical switching, to anticipate a potentially more sensitive PSA target relationship. A linear fit to the photoelectric signal generated by the capacitor-amplified target was performed and the linear regression equation was found to be consistent with I (μA) = 7.6684 × log $C_{[PSA]}$ + 15.744 (ng mL^{-1}, R^2 = 0.9886, n = 10). Comparison with direct measurements of the PEC without capacitor amplification showed a linear regression equation of I (nA) = 86.116 × log $C_{[PSA]}$ + 181.9 (ng mL^{-1}, R^2 = 0.9916, n = 10). Because the capacitor was able to collect and instantaneously release the photocurrent, the sensitivity of the converted digital signal generated per unit PSA was 89 times greater than that without capacitor amplification, which was of great significance for the sensitive detection of trace disease-associated proteins.

In addition, the PEC assay system enhanced by the piezoelectric effect was comparable to commercially available PSA ELISA kits such as 0.1 ng mL^{-1} for Sangon Biotech (cat#: D721133); 94 pg mL^{-1} for FineTest (cat#: EM1314), 39 pg mL^{-1} for Abcam (Cat#: ab264615) in terms of sensitivity and response to PSA. More meaningfully, this PEC sensing platform coupled the magnetic separation device, an ultrasound generator, and a PEC test device in a miniaturized test box, addressing the need for miniaturization and portability of PEC testing in community healthcare and POCT. In addition, the constructed test platform had a significant advantage in terms of cost per test compared to commercially available related ELISA kits, the costing of which is further described in the Supporting Information.

Another issue worth exploring was whether the test platform was selective and stable. Classical spiked recovery experiments

https://doi.org/10.1021/acs.analchem.2c00066
Anal. Chem. 2022, 94, 3418−3426

of nontargeted samples were used to probe the selectivity of this sensing platform. In detail, the target concentration of PSA in the experiment was set at 4.0 ng mL^{-1}, mainly because this concentration tends to be used as an indicator of the likelihood of having prostate cancer in medicine. The concentration of other disease-related protein molecules such as CEA, carcinoembryonic antigen 15-3 (CA 15-3), IgG, and AFP was set at 10 times the concentration of the target PSA (40 ng mL^{-1} or 40 U mL^{-1}). As shown in Figure 5E, the nontarget proteins did not cause changes in photocurrent, except for the mixed samples as well as the target PSA, which exhibited significant photocurrent, indicating that the platform had good selectivity. The stability of the CAAB test system depends mainly on the stability of the electrodes and capacitors. Therefore, the stability of the electrodes was approved by a 30 day photocurrent test. As shown in Figure 5F, the stability of the electrodes was illustrated by the fact that there was no significant decay in the change of current during the four weeks of testing. Last but not least, to investigate the consistency of the piezoelectric assisted enhanced PEC device with the kit assay, a series of PSA standard buffer solutions of known concentrations (0.1−20 ng mL^{-1}) were configured and assayed in parallel by both methods, and the respective assay results were plotted as variables in a curve as shown in Figure 5G. The calculated Pearson coefficient was 0.9968 ($p < 0.958$), indicating that the two methods showed good correlation in the range of PSA targets tested, and the corresponding computational method expression is provided in the Supporting Information.

The accuracy of the PEC biosensor platform based on the piezoelectric enhancement effect on actual samples of human serum was evaluated to fulfill the needs of the developed CAAB assay in practical scenarios of POCT and community medicine. The comparison protocol, similarly, was compared with a commercially available human PSA ELISA kit, and the test samples were obtained from the local hospital. The test results are shown in Table S1. Impressively, t_{exp} values were calculated to be <2.77 for all tested specimens ($t_{crit\ [0.05,4]}$ = 2.77) based on two methods, which further demonstrated the promising application and potential. Likewise, it illustrated the potential of the novel test system contributed in this work for testing in POCT and physician office scenarios.

CONCLUSIONS

In this work, we have successfully developed a novel PEC immunoassay based on the piezophototronic-assisted effect for the sensitive detection of PSA. Nanocubic blocks of $NaNbO_3$ are characterized as showing good piezoelectric properties. Through the ultrasound-induced piezoelectric effect, the rapid separation of electrons and holes occurs for the rapid depletion of AA generated by PSA incubation for conversion to an excellent photoelectric signal. The highlights of this paper are mainly the following aspects: (i) the successful construction of PEC test platform with a highly integrated continuous feed system, magnetic separation system, and piezoelectric generation system; (ii) the construction of a cost-controlled and stable portable PEC test system for POCT in the developing countries; and (iii) the integration of capacitor amplification for sensitive and rapid clinical testing. This is a study with lessons learned and commercial implications, which has strong applicability and demand in POCT testing scenarios, community healthcare, and resource-limited areas.

ASSOCIATED CONTENT

Supporting Information

The Supporting Information is available free of charge at https://pubs.acs.org/doi/10.1021/acs.analchem.2c00066.

Chemical and reagents, instruments, preparation of mAb_1-MB immunosensing probe, preparation of anti-PSA−SiO_2−ALP, fabrication of paper-based sandwich capacitor, cost accounting, and Pearson test calculation (PDF)

AUTHOR INFORMATION

Corresponding Authors

Xiaolong Liu − *The United Innovation of Mengchao Hepatobiliary Technology Key Laboratory of Fujian Province, Mengchao Hepatobiliary Hospital of Fujian Medical University, Fuzhou 350025, People's Republic of China;* orcid.org/0000-0002-3096-4981; Phone: +86-591-2286 6125; Email: xiaoloong.liu@gmail.com; Fax: +86-591-2286 6135

Dianping Tang − *Key Laboratory of Analytical Science for Food Safety and Biology (MOE & Fujian Province), Department of Chemistry, Fuzhou University, Fuzhou 350108, People's Republic of China;* orcid.org/0000-0002-0134-3983; Email: dianping.tang@fzu.edu.cn

Authors

Zhichao Yu − *Key Laboratory of Analytical Science for Food Safety and Biology (MOE & Fujian Province), Department of Chemistry, Fuzhou University, Fuzhou 350108, People's Republic of China*

Hexiang Gong − *Key Laboratory of Analytical Science for Food Safety and Biology (MOE & Fujian Province), Department of Chemistry, Fuzhou University, Fuzhou 350108, People's Republic of China*

Jianhui Xu − *Key Laboratory of Analytical Science for Food Safety and Biology (MOE & Fujian Province), Department of Chemistry, Fuzhou University, Fuzhou 350108, People's Republic of China*

Yuxuan Li − *Key Laboratory of Analytical Science for Food Safety and Biology (MOE & Fujian Province), Department of Chemistry, Fuzhou University, Fuzhou 350108, People's Republic of China*

Yongyi Zeng − *The United Innovation of Mengchao Hepatobiliary Technology Key Laboratory of Fujian Province, Mengchao Hepatobiliary Hospital of Fujian Medical University, Fuzhou 350025, People's Republic of China*

Complete contact information is available at: https://pubs.acs.org/10.1021/acs.analchem.2c00066

Notes

The authors declare no competing financial interest.

ACKNOWLEDGMENTS

We gratefully acknowledge the financial support from the National Natural Science Foundation of China (21874022 and 21675029).

REFERENCES

(1) Zhao, W.-W.; Xu, J.-J.; Chen, H.-Y. *Chem. Soc. Rev.* **2015**, *44*, 729−741.

(2) Zhao, W.-W.; Xu, J.-J.; Chen, H.-Y. *Anal. Chem.* **2018**, *90*, 615−627.

(3) Zhao, C.-Q.; Ding, S.-N. *Coord. Chem. Rev.* **2019**, *391*, 1−14.
(4) Ye, X.; Wang, X.; Kong, Y.; Dai, M.; Han, D.; Liu, Z. *Angew. Chem., Int. Ed.* **2021**, *60*, 11774−11778.
(5) Xiang, Y.; Kong, Y.; Feng, W.; Ye, X.; Liu, Z. *Chem. Sci.* **2021**, *12*, 12977−12984.
(6) Shi, L.; Yin, Y.; Zhang, L.-C.; Wang, S.; Sillanpää, M.; Sun, H. *Appl. Catal., B* **2019**, *248*, 405−422.
(7) Li, F.; Zhou, Y.; Yin, H.; Ai, S. *Biosens. Bioelectron.* **2020**, *166*, 112476.
(8) Zhou, Q.; Tang, D. *TrAC, Trends Anal. Chem.* **2020**, *124*, 115814.
(9) Zhu, L.-B.; Wang, H.-Y.; Zhang, T.-Y.; Chen, F.-Z.; Han, D.-M.; Zhao, W.-W. *Anal. Chem.* **2021**, *93*, 15761−15767.
(10) Hao, M.; Miao, P.; Wang, Y.; Wang, W.; Ge, S.; Yu, X.; Hu, X.-X.; Ding, B.; Zhang, J.; Yan, M. *Anal. Chem.* **2021**, *93*, 11251−11258.
(11) Khan, S.; Lemes Ruwer, T.; Khan, N.; Köche, A.; Lodge, R. W.; Coelho-Júnior, H.; Sommer, R. L.; Leite Santos, M. J.; Malfatti, C. F.; Bergmann, C. P.; Fernandes, J. A. *J. Mater. Chem. A* **2021**, *9*, 12214−12224.
(12) Cao, J.-T.; Ma, Y.; Lv, J.-L.; Ren, S.-W.; Liu, Y.-M. *Chem. Commun.* **2020**, *56*, 1513−1516.
(13) Dong, W.; Li, Z.; Wen, W.; Liu, B.; Wen, G. *ACS Appl. Mater. Interfaces* **2021**, *13*, 57497−57504.
(14) Luo, Z.; Zhang, L.; Zeng, R.; Su, L.; Tang, D. *Anal. Chem.* **2018**, *90*, 9568−9575.
(15) Lv, S.; Zhang, K.; Zhu, L.; Tang, D. *Anal. Chem.* **2020**, *92*, 1470−1476.
(16) Yang, R.; Yan, X.; Li, Y.; Zhang, X.; Chen, J. *ACS Appl. Mater. Interfaces* **2017**, *9*, 42482−42491.
(17) Lou, S.; Zhou, Z.; Shen, Y.; Zhan, Z.; Wang, J.; Liu, S.; Zhang, Y. *ACS Appl. Mater. Interfaces* **2016**, *8*, 22287−22294.
(18) Zhou, Q.; Li, G.; Chen, K.; Yang, H.; Yang, M.; Zhang, Y.; Wan, Y.; Shen, Y.; Zhang, Y. *Anal. Chem.* **2020**, *92*, 983−990.
(19) Yang, H.; Zhou, Q.; Fang, Z.; Li, W.; Zheng, Y.; Ma, J.; Wang, Z.; Zhao, L.; Liu, S.; Shen, Y.; Zhang, Y. *Chem* **2021**, *7*, 2708−2721.
(20) Yang, Z.; Zhang, Y.; Schnepp, Z. *J. Mater. Chem. A* **2015**, *3*, 14081−14092.
(21) Xue, H.; Chen, K.; Zhou, Q.; Pan, D.; Zhang, Y.; Shen, Y. *J. Mater. Chem. B* **2019**, *7*, 6789−6795.
(22) Yu, Z.; Xu, J.; Li, Y.; Gong, H.; Wei, Q.; Tang, D. *J. Mater. Chem. C* **2021**, *9*, 14351−14358.
(23) Yu, L.-M.; Zhu, Y.-C.; Liu, Y.-L.; Qu, P.; Xu, M.-T.; Shen, Q.; Zhao, W.-W. *Anal. Chem.* **2018**, *90*, 10803−10811.
(24) Yu, Y.; Wang, X. *Adv. Mater.* **2018**, *30*, 1800154.
(25) Chen, Y.; Wang, L.; Gao, R.; Zhang, Y.-C.; Pan, L.; Huang, C.; Liu, K.; Chang, X.-Y.; Zhang, X.; Zou, J.-J. *Appl. Catal., B* **2019**, *259*, 118079.
(26) Liu, Z.; Wang, L.; Yu, X.; Zhang, J.; Yang, R.; Zhang, X.; Ji, Y.; Wu, M.; Deng, L.; Li, L.; Wang, Z. L. *Adv. Funct. Mater.* **2019**, *29*, 1807279.
(27) Singh, S.; Khare, N. *Nano Energy* **2017**, *42*, 173−180.
(28) Yu, D.; Liu, Z.; Zhang, J.; Li, S.; Zhao, Z.; Zhu, L.; Liu, W.; Lin, Y.; Liu, H.; Zhang, Z. *Nano Energy* **2019**, *58*, 695−705.
(29) Liu, H.; Wu, H.; Ong, K. P.; Yang, T.; Yang, P.; Das, P. K.; Chi, X.; Zhang, Y.; Diao, C.; Wong, W. K. A.; Chew, E. P.; Chen, Y. F.; Tan, C. K. I.; Rusydi, A.; Breese, M. B. H.; Singh, D. J.; Chen, L.-Q.; Pennycook, S. J.; Yao, K. *Science* **2020**, *369*, 292−297.
(30) Shrivastava, S.; Trung, T. Q.; Lee, N.-E. *Chem. Soc. Rev.* **2020**, *49*, 1812−1866.
(31) Wang, Y.; Zhou, J.; Li, J. *Small Methods* **2017**, *1*, 1700197.
(32) Ge, L.; Wang, P.; Ge, S.; Li, N.; Yu, J.; Yan, M.; Huang, J. *Anal. Chem.* **2013**, *85*, 3961−3970.
(33) Zhou, Q.; Lin, Y.; Zhang, K.; Li, M.; Tang, D. *Biosens. Bioelectron.* **2018**, *101*, 146−152.
(34) Lan, F.; Sun, G.; Liang, L.; Ge, S.; Yan, M.; Yu, J. *Biosens. Bioelectron.* **2016**, *79*, 416−422.
(35) Cheng, Q.; Feng, J.; Wu, T.; Zhang, N.; Wang, X.; Ma, H.; Sun, X.; Wei, Q. *Anal. Chem.* **2021**, *93*, 13680−13686.
(36) Feng, J.; Li, N.; Du, Y.; Ren, X.; Wang, X.; Liu, X.; Ma, H.; Wei, Q. *Anal. Chem.* **2021**, *93*, 14196−14203.
(37) Feng, J.; Wu, T.; Cheng, Q.; Ma, H.; Ren, X.; Wang, X.; Lee, J. Y.; Wei, Q.; Ju, H. *Lab Chip* **2021**, *21*, 378−384.
(38) Mao, X.; Zhang, C. *Talanta* **2022**, *238*, 123052.
(39) Browne, M. P.; Plutnar, J.; Pourrahimi, A. M.; Sofer, Z.; Pumera, M. *Adv. Energy Mater.* **2019**, *9*, 1900994.
(40) Li, X.; Pan, X.; Lu, J.; Zhou, Y.; Gong, J. *Biosens. Bioelectron.* **2020**, *158*, 112158.
(41) Zhang, K.; Lv, S.; Tang, D. *Anal. Chem.* **2019**, *91*, 10049−10055.
(42) Qiu, Z.; Shu, J.; Liu, J.; Tang, D. *Anal. Chem.* **2019**, *91*, 1260−1268.
(43) Jeong, S.; Park, J.; Pathania, D.; Castro, C. M.; Weissleder, R.; Lee, H. *ACS Nano* **2016**, *10*, 1802−1809.
(44) Zeng, R.; Wang, W.; Chen, M.; Wan, Q.; Wang, C.; Knopp, D.; Tang, D. *Nano Energy* **2021**, *82*, 105711.
(45) Singh, S.; Khare, N. *Nano Energy* **2017**, *38*, 335−341.
(46) Yu, Z.; Gong, H.; Li, Y.; Xu, J.; Zhang, J.; Zeng, Y.; Liu, X.; Tang, D. *Anal. Chem.* **2021**, *93*, 13389−13397.
(47) Hu, Y.; Chen, W.; Wang, S.; Zhang, F.; Song, W.; Wang, L.; You, S. *Int. J. Hydrogen Energy* **2021**, *46*, 29994−30004.
(48) Reza Gholipour, M.; Dinh, C.-T.; Béland, F.; Do, T.-O. *Nanoscale* **2015**, *7*, 8187−8208.
(49) Marschall, R. *Adv. Funct. Mater.* **2014**, *24*, 2421−2440.

https://doi.org/10.1021/acs.analchem.2c00066
Anal. Chem. 2022, 94, 3418−3426